Noname manuscript No.
(will be inserted by the editor)

Slackwater sediments record the increase in sub-daily rain flood due to climate change in a European Mediterranean catchment

J.D. Moral-Erencia · P. Bohorquez · P.J. Jimenez-Ruiz · F.J. Pérez-Latorre

Received: : 26 November 2019 / Accepted: 10 May 2020 / Published online: 4 June 2020

Abstract In this work we propose an original method to determine the magnitude of the discharge, the intensity of the precipitation and the duration of short-rain floods in small torrential basins (<2000 km^2), extending our earlier approach for long-rain floods in larger basins (Water 2016, 8, 526; Remote Sens. 2017, 9, 727). The studied areas are located in ungauged catchments with high erosion rates where torrents deposit slackwater sediments near the outlet of the basins. Such deposits and erosive morphologies allow us to analyse sub-daily extreme hydrological events by combining standard techniques in paleohydrology, the kinematic wave method and remote-sensed paleostage indicators. The formulation was correctly verified in extreme events through reliable gauge measurements and a high-resolution distributed hydrological model showing the accuracy of our calculations (10% $\leq$ relative error $\leq$ 22%). In catchments of the European Mediterranean region where the frequency and magnitude of short-rain floods are increasing (e.g. the Guadalquivir Basin), the main hydrological variables can thus be quantified post-event using the proposed approach. The outputs may serve to construct a new database for this kind of events complementary to the existing daily database for long-rain floods (>24 h). The need is evident for safety designs of civil infrastructures and flood risk mitigation strategies in the current climate change scenario.

Keywords short-rain flood · satellite imagery · flood monitoring · paleohydrology · climate change · Guadalquivir basin

J.D. Moral-Erencia · P. Bohorquez
Centro de Estudios Avanzados en Ciencias de la Tierra (CEACTierra), Universidad de Jaén. Campus de las Lagunillas, 23071 Jaén, Spain Tel.: +34-953-21287

P.J. Jimenez-Ruiz · F.J. Pérez-Latorre
Área de Mecánica de Fluidos, Dpto Ingeniería Mecánica y Minera, Universidad de Jaén, Campus Científico Tecnológico de Linares, 23700 Linares, Spain

del Moral-Erencia J.D., Bohorquez P., Jiménez-Ruíz P.J., Pérez-Latorre F.J. Slackwater sediments record the increase in sub-daily rain flood due to climate change in a European Mediterranean catchment. Water Resources Management, 34: 4431-4447, 2020. T1 Q2 (37/137 Civil Engineering, IF 2020=3.5).

1 Introduction

The study of inundation events with a duration lower than 1-day, referred to as short-rain flood in Merz and Blöschl (2003), is acquiring relevancy in the actual climate change scenario (e.g. Bellos and Tsakiris, 2016; García-Feal et al., 2018; Bellos et al., 2020). The climate predictions establish a reduction of the total amount of precipitation with a higher spatial concentration (IPCC, 2013), especially in the Mediterranean area of Europe (EEA, 2017). We expect an increase in the frequency and magnitude of sub-daily flood events (Alfieri and Thielen, 2015), human and direct-indirect economic losses (Dottori et al., 2018). Actual predictions were confirmed during the 2009-2011 period that exhibited a remarkable record of sub-daily floods in European Mediterranean basins (Fig. 1a). Furthermore, a European Flood Awareness System was developed, requiring quantitative streamflow data in ungauged rivers for validation purpose (Alfieri et al., 2016).

In this paper, we originally reconstruct the characteristics of extreme sub-daily hydrological events in small ungauged basins (<2000 km^2) by inferring not only the hydraulic parameters (e.g. discharge) but also hydrologic variables (i.e. rainfall intensity and duration of the event) using remote sensed HWM-PSI (High Water Marks - PaleoStage Indicators). Taking into account the importance of the availability of probable maximum precipitation (PMP) data in civil engineering designs, the hydrologic information derived from the current approach is useful to design civil safety infrastructures as well as to mitigate flood risk (Díez-Herrero et al., 2008). Our new approach extends the capabilities and applicability of our former method (Bohorquez, 2016; Bohorquez and del Moral-Erencia, 2017), initially planned for long-rain floods in larger basins.

The starting point is that short-rain floods sculpt a variety of elements of the drainage system at different spatial scales, from gullies to ephemeral torrents (Jacobson et al., 2016). Post-event sedimentological and botanical flood evidence, channel shape and bed slope record the magnitude of the event that can be inferred using standard techniques of paleohydrology (e.g. Baker, 2008; Carling et al., 2009). Traditionally, applications of paleohydrology have been limited to catastrophic flooding of large rivers and ignored the challenge of studying lesser extent morphodynamic processes (Naylor et al., 2017). The availability of high-resolution altimetry data and satellite imagery may, however, allow the geometrical modelling of narrow channels and the positioning of HWM-PSI in small ungauged basins. By combining the inferred peak discharge with an analytical hydrological model (Brutsaert, 2005; Mays, 2010), the outputs may also include the mean intensity and duration of the rainfall event.

The paper is organised as follows: Materials and Methods are presented in § 2. Experimental and numerical results are described in § 3. We focus on the verification of the proposed method in a simple, gauged basin (§ 3.1), and later apply the same procedure in more complex floodplains (§ 3.2) and steep torrents (§ 3.3). Finally, we draw some conclusions in § 4.

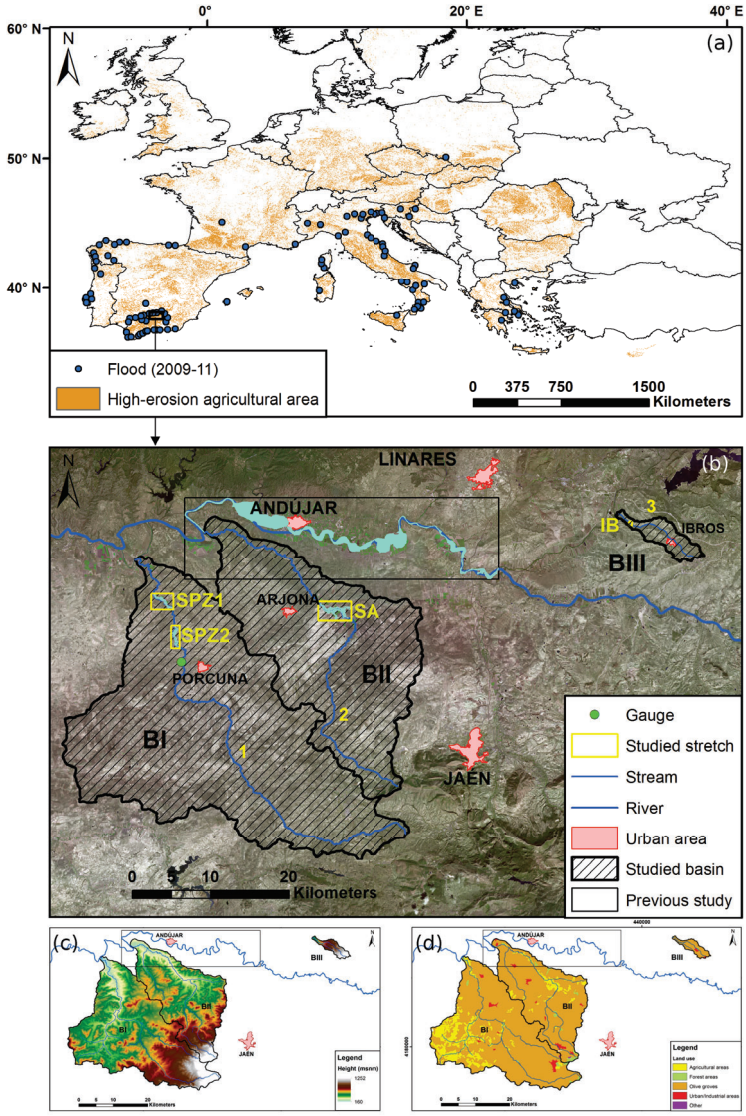

Fig. 1 (a) Map of agricultural areas in Europe under high-erosion risk ($\geq$10 t·h^{-1}·y^{-1}), coloured in orange, and floods detected by Alfieri and Thielen (2015) during the period 2009-11 in these areas, indicated with a dark blue circle. (b) General view of the study areas along the Guadalquivir Basin. The non-regulated basins described in this paper are highlighted with a striped pattern. They are referred to as Salado de Porcuna (BI), Salado de Arjona (BII) and Ibros (BIII). The most important rivers, torrents and streams are indicated in dark blue, and the analysed stretches are marked with yellow rectangles that include the inundated areas in light blue. Representative urban areas are coloured in light red. (c) Hypsometric and (d) land use maps in the studied basins. The rectangle in black in panels (b)-(d) shows the area studied in our earlier works (Bohorquez, 2016; Bohorquez and del Moral-Erencia, 2017).

2 Materials and Methods

2.1 Study site

The selected study area is located in the southwest of Europe (Fig. 1), within the upper Guadalquivir Basin (Spain). It comprises three sub-basins associated with the tributary fluvial courses referred to as Salado de Porcuna, Salado de Arjona and Arroyo de Ibros; denoted as BI, BII and BIII in Fig. 1b. The torrential nature of such catchments, as well as many other ungauged tributary basins southern to the Guadalquivir River, requires the reconstruction of short rain floods by using paleohydraulic methods to design flood mitigation strategies by competent authorities.

The Mediterranean climate frames the study sites, characterised by the seasonal and irregular distribution of rainfall. The complex topography of the landscapes and the geographical position, recall Fig. 1, favour the presence of different climate influences coming from the Mediterranean Sea and the Atlantic Ocean. Two kinds of precipitation/flood events developed. First, continuous rainfalls longer than one week provoke extreme inundations at the basin scale (long-rain floods) as described in our previous works (Bohorquez, 2016; Bohorquez and del Moral-Erencia, 2017). Second, brief and intense rainfalls (< 24 h) produced by reduced area storms induce local floods at the sub-basin scale (short-rain floods). BI-BIII have suffered frequent floods during the last decades. In BI and BII, extreme hydrological events occurred in 1996, 1999, 2001, 2003, 2007, 2008, 2009, 2010, 2012, 2016 and 2018, the most dangerous on 26-12-2009. In BIII, the most significant event occurred on 15-09-2009 and caused economic losses above 1M€.

BI and BII have a size of 809 and 490 km^2, respectively, while BIII is much smaller (25.6 km^2), leading in both cases to a sub-daily time of concentration. In BI-BII the flow is subcritical due to the low bed slope (1%), bankfull depth is ≈ 3 m, bankfull width lies around 39.8 m (BI) and 26.7 m (BII), see Table 1. Such properties vary in basin BIII where bankfull depths and widths are 1.8-3.2 m and 9.6-19.1 m, respectively, and steep slopes of 3.5% along the streams and 17% across the basin provoke supercritical flows. Regarding the width of the inundated floodplains, we found 243-470 m (BI), 198-660 m (BII) and much narrower values of 22-59 m in BIII.

The study basins mimic an ideal laboratory with a homogeneous surface but at a much larger, real scale. Olive groves dominate the soil use, occupying 84.5% (BI), 91.1% (BII) and 94.6% (BIII) of the drainage area. The combination of steep slopes (Fig. 1c) and land use of olive groves under conventional tillage (Fig. 1d) causes a high incidence of laminar and gully water erosion processes, aggravated in site III due to the more significant role of both factors. The absence of dams across the fluvial courses ensures that the flow responds naturally to the torrential rainfall registered over the basin. The fine granulometry of available sediments favours transport processes dominated by wash load that settle slackwater deposits where flow velocity is low. In erosive stretches, the steep slope and high availability of vegetation make possible to

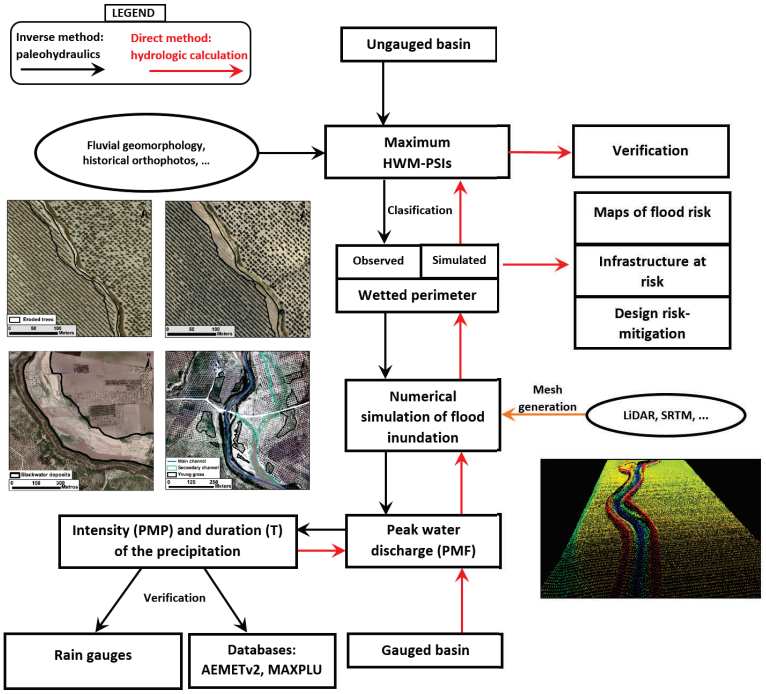

Fig. 2 Flowchart summarising the methods used in this work. Arrows in red and black colour highlight the direct and inverse methods, respectively. Orange arrows indicate a step common in both methods.

infer the inundated area according to botanical evidence as scour of trees on stream bank (Bodoque et al., 2005).

We chose four stretches of the three main rivers within BI-BIII, see Fig. 1b. In BI, we selected two sub-areas (yellow squares) located downstream of a gauging station (green bullet). In BII, the stretch is located in an intricate floodplain representing the confluence of several courses and exhibits a nick point with discontinuous bed slope that provokes the inundation of floodplains and deposition of slackwater sediments. Finally, in BIII, we chose a small area situated downstream from the village of Ibros (red area) where high-speed flows induce erosive processes.

2.2 Overview of the methods: Direct and Inverse problems

We consider two kinds of hydrological problems, as sketched in Fig. 2:

– In the direct problem, the input data is the known discharge (gauged basin) or precipitation. The primary output data of the computational model is the inundated area by the flood (Bohorquez, 2016; Bohorquez and del Moral-Erencia, 2017). The numerical simulation of flooding areas is

commonly done with the 2D unsteady shallow-water equations. We adopt the novel software Iber+ that accelerates the simulation by a factor of 100 using a graphics processing unit rather than a central processing unit (García-Feal et al., 2018).

– In the inverse problem, the flooded area is delimited post-event using available remote sensed HWM-PSIs, but the peak flow discharge is unknown (ungauged basin). Detected PSIs are slackwater deposits, growth of young grass, secondary channels and scoured olive trees. By applying standard methods of paleohydrology, we then infer the peak water discharge as an output (Bohorquez and Darby, 2008). Here we propose a novel way to determine the inundated area through botanical and sedimentary evidence from high-resolution satellite imagery (< 1 m of ground sampling distance). Lastly, we correlate the spatial-averaged rainfall of the event with the inferred discharge and the drainage area of the upstream basin.

In BI, the availability of streamflow data allowed us to run the direct method. Hydraulic data was downloaded from an open hydrologic information system (http://sig.magrama.es/aforos). We selected the gauging station number 5142 (green bullet in Fig. 1b) which recorded water discharge and flow depth in the period 1980-2018. The flood-prone area, A_{mod}, was simulated for a known water discharge by using Iber+ (García-Feal et al., 2018). The two river stretches SPZ1 and SPZ2 in BI (Fig. 1b) required, therefore, two simulations (Table 1). Subsequently, the analysis and classification of the HWM-PSIs allowed the delimitation of the observed inundated extent, A_{obs}. The classification of HWM-PSIs was according to the origin (botanical or geological) and typology (erosive or sedimentary) of the evidence. Finally, we computed the critical success index (CSI) as a measurement of the quality of the simulated inundation (Bates and De Roo, 2000),

$$\mathrm{CSI} = \frac{A_{\mathrm{obs}} \cap A_{\mathrm{mod}}}{A_{\mathrm{obs}} \cup A_{\mathrm{mod}}}\,, \tag{1}$$

where A_{obs} and A_{mod} represent the sets of pixels observed to be inundated and predicted as inundated, respectively. This index quantifies the overlap between the observed and simulated wetted perimeters and varies in the 0-1 range. A value close to 0 indicates that no correlation exists between simulated and observed extents, while near 1 implies a perfect agreement. According to previous flood simulation studies, there are a relatively small number of simulations with $\mathrm{CSI} > 0.7$ (Wood et al., 2016). We were able to achieve excellent agreements with $0.85 \leq \mathrm{CSI} \leq 0.9$.

In the ungauged BII-III, we applied the inverse method to retrodict the probable maximum flood (PMF), the probable maximum precipitation (PMP) and the duration of the event (T) as output products (see Table 2). The first step consists of searching and classifying a set of remote sensed paleostage indicators in the historical orthophotography registry. Such HWM-PSIs provide accurate information of the observed wetted area A_{obs}. Secondly, we

defined the PMF as the discharge that maximises the CSI for a wide range of possible streamflows. The CSI was evaluated for each simulated extent A_{mod}, selecting the optimal value that exhibits the best correlation between the simulated and observed areas. To find the optimal value, the discharge was increased monotonously which required between 12 and 14 simulations in both basins (Table 1). Then, the spatial-averaged PMP was obtained from the drainage area of the upstream basin, A_{drain}, and the inferred PMF under the condition of saturation of surface soils observed in the reconstructed floods:

$$\mathrm{PMP} = \frac{\mathrm{PMF}}{A_{\mathrm{drain}}} \,. \tag{2}$$

Later, we estimated the minimum duration of the event, given by time of concentration T, using the kinematic wave (or rational) method (Brutsaert, 2005):

$$\mathrm{T} = \frac{L}{U_{\mathrm{PMP}}} \,, \tag{3}$$

where L is the characteristic length of the catchment (e.g. $L = A_{\mathrm{drain}}^{1/2}$ in a nearly square basin as BI and BII) and U_{PMP} is the runoff velocity (Mays, 2010):

$$U_{\mathrm{PMP}} = \left(\frac{\mathrm{PMP} \cdot L}{3.6 \cdot 10^6} \right)^{\frac{2}{5}} \cdot S_0^{\frac{3}{10}} \cdot n^{-\frac{3}{5}} \,. \tag{4}$$

In (4), S_0 is the mean slope of the basin and $n = 0.025$ s·m$^{-1/3}$ corresponds to the Manning's roughness coefficient characteristic of silt and clay.

To ensure accuracy in the computation of the flooded areas A_{mod} (direct and inverse problem) and the inferred water discharge PMF (inverse problem), we used a high-resolution mesh based on LiDAR (Light Detection and Ranging) elevations. LiDAR cloud points dated in 2014 were downloaded from the Spanish Geographic Institute (http://pnoa.ign.es/). In doing so, we maximised the reliability of channel geometry in the numerical simulation (Bates and De Roo, 2000). A non-structured computational mesh was then required. The size of the computation domains in the simulated river stretches varied according to their inundation extents (yellow rectangles in Fig. 1b), requiring a balance between area and spatial resolution. The specific characteristics and boundary conditions of the two-dimensional numerical simulations are indicated in Table 1.

Lastly, existing databases on peak river discharges (CAUMAX by CEDEX, 2014) and daily rainfall depths (AEMETv2, see Peral-García et al., 2017) are later used to discuss the relevance of the outputs of our approach. On the one hand, the expected discharge of rivers in the Guadalquivir Basin were evaluated for different return periods using the correlations by CAUMAX, as established in the Directive FOM/298/2016 of the Spanish Government for the design of drainage systems in civil infrastructures (https://www.boe.es/). On the other hand, AEMETv2 provided the daily accumulated precipitation for the period 1951-2019 with a spatial resolution of 5 km based on 2300 rain gauges non-uniformly distributed across Spain.

Table 1 Main parameters in the river stretches and basins.

	BI	BII	BIII
Number of simulations	2	12	14
Number of inflows	1	4	1
Inflow boundary condition	Discharge	Discharge	Discharge
Number of outflows	1	1	1
Outflow boundary condition	Water depth	Water depth	Free discharge
Flow regime	Subcritical	Subcritical	Supercritical
Manning's coefficient ($s \cdot m^{-1/3}$)	0.025	0.025	0.025
Mesh resolution (m)	5	3	0.5
Mesh nodes	77724-78133	638883	108907
Mesh elements	153918-154714	1272165	131307
Drainage area (km^2)	808	490	25.6
Average slope (°)	6.4	7.03	9.76
Average bed slope (°)	0.69	0.62	2.04
Bankfull depth (m)	39.8	26.7	9.6-19.1
Floodplain width (m)	243-470	198-660	22-59
Olive grove soil use (%)	84.5	91.1	94.6

3 Results

3.1 Verification of the Direct Method in a Gauged Basin (BI)

Here we benchmark the accuracy of the hydraulic model used to numerically simulate the flooding area at a prescribed water discharge PMF in a gauged basin. We refer this procedure to as direct calculus because the local values of hydrologic variables (i.e. water discharge, water surface elevation and bed topography) are well known. The inundated area can also be accurately inferred post-event from remote sensing data, to be compared with the simulated one, allowing us to check the accuracy of the numerical simulation. Also, the average rainfall intensity PMP and minimum duration of the event T are obtained from (2) and (3)-(4), respectively. We show the extreme nature of such a short rain event by discussing the relative importance of the ensuing discharge and daily precipitation depth against the complete datasets available in Spain since 1950, namely CAUMAX (CEDEX, 2014) and AEMETv2 (Peral-García et al., 2017), respectively.

The studied flood occurred in December 2009 at the river stretches SPZ1 (Figs. 3a-b) and SPZ2 (Figs. 3c-d), see their locations near the BI outlet in Fig. 1b. Fig. 3a (SPZ1) and Fig. 3c (SPZ2) show PSIs classified according to the nature of the evidence from the Digital Globe satellite image (09/05/2011) and local orthophotos (PNOA, 07/2011). Slackwater deposits of fine sediments (yellow), scoured olive trees (pink), young grass at local hills (green) and secondary channels (light blue) delimitate the inundated areas. The main channel and the extension of the floodplains are also shown in dark blue and black solid line in Figs. 3a and 3c.

Slackwater sediments are the most abundant evidence, representing more than 64% of the field evidence. Young grass grew at the top of sediment bumps which are distributed randomly in the inundated floodplains (16.8%). Such

Table 2 Water discharge (PMF), probable maximum precipitation (PMP) and minimum duration of the event (T). In BII-III, we solved the inverse problem sequentially and analysed multiple sub-basins with different sizes (denoted from I to IV). Also included are the 200yr (PMF_{200}) and 500yr (PMF_{500}) return-period discharges given by the national CAUMAX database (CEDEX, 2014), as well as the daily precipitation depth according (DPD) according to AEMETv2 (Peral-García et al., 2017).

	A_{drain} km^2	PMF m^3·s^{-1}	PMP mm·h^{-1}	T h	PMF_{200} m^3·s^{-1}	PMF_{500} m^3·s^{-1}	DPD mm	T×PMP mm
Porcuna	670	533	2.9	7.1	302	444	44.4	20.6
Arjona	307	460	5.4	5.6	141	199	45.7	30.2
I	87.2	195	8.1	5.6	-	-	-	-
II	191	180	3.4	5.6	-	-	-	-
III	15.3	45	10.6	5.6	-	-	-	-
IV	13.7	40	10.5	5.6	-	-	-	-
Ibros	23.3	170	26.3	1.9	183	211	32.1	50
I	0.41	1.5	13	1.9	-	-	-	-
II	0.66	4.5	24.6	1.9	-	-	-	-
III	1.54	4.1	9.6	1.9	-	-	-	-
IV	0.26	2.7	37.4	1.9	-	-	-	-

a botanical evidence is only visible in the studied river reaches and, hence, it represents a clear flood record. Meandering secondary channels were also eroded in some regions of the floodplains (11.9%) by high-speed flows. The sculpted channels can be appreciated even in the LiDAR data given their dimensions. Lastly, the comparison of pre- and post-inundation orthophotos shows the erosion of multiple olive trees across 6.9% of the inundated area.

The inset of Fig. 3b shows the peak river discharge (PMF = 533 m^3·s^{-1}) and flow depth (2.85 m) on the 26th December 2009. The measured hydrograph (blue line) exhibits a nearly symmetrical shape with a duration of the rising limb and recession of 7.5 ± 0.5 h. Peak values were sustained during a plateau of 3 hours. Hence, the rainstorm lasted about 10.5 h. The maximum flow depth was of the same order as for the most dangerous flood in 2007 (i.e. 3 m, see the inset of Fig. 3a) when the discharge was 643 m^3·s^{-1} (Fig. 4a). The reconstructed inundation was the second most extreme event documented in the basin, proving the extreme nature of the short-rain flood.

Maps of the simulated flow depth are depicted in Fig. 3b and 3d. For the sake of the comparison with the observed, flooded area, the thick solid line in black depicts the inundated perimeter from the remote sensed paleostage indicators (Fig. 3a and 3c). There is an excellent agreement between both results. In both river reaches the flow depth achieved maximum values in the main channel (approximately, 5 m), and it was much shallower in the floodplains (about 1 m). Secondary channels eroded by the flood wave are 2 m depth. Note that the numerical simulation reproduces the secondary channels observed in the orthophotos.

To quantify the accuracy of the numerical simulation, we evaluated the CSI given by (1), which yield CSI = 0.90 (SPZ1) and 0.85 (SPZ2). The proximity to the perfect agreement (CSI = 1) highlights the quality of our numerical simulation. Thanks to the high-resolution LiDAR and the homogeneity of the

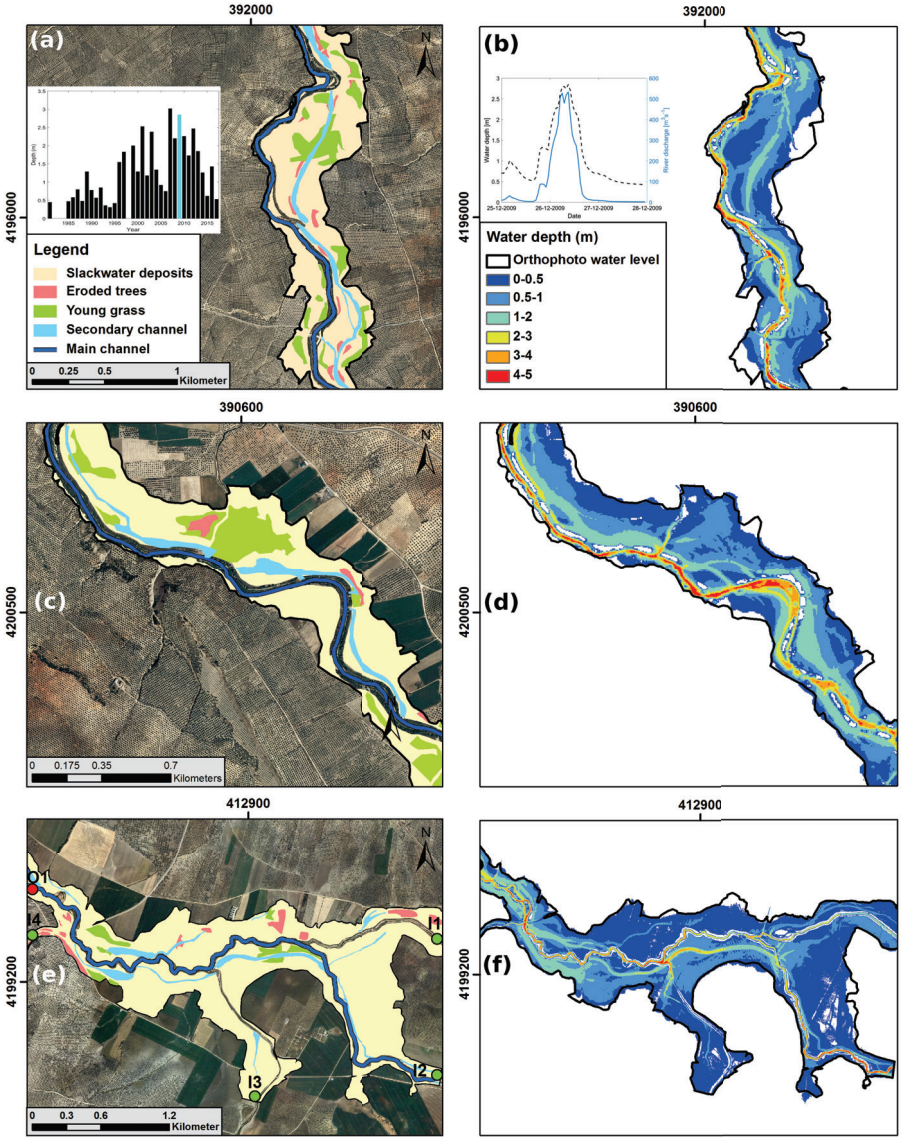

Fig. 3 Results in the (a-d) gauged basin BI and (e-f) ungauged basin BII: (a, c, e) remote sensed HWM-PSIs from satellite imagery (Digital Globe, 09/05/2011) and local orthophotos (PNOA, 07/2011); (b, d and f) simulated flow depth. The inset of panel (a) shows the maximum flow depth per year since 1980 measured at the gauge station. The inset of panel (b) depicts the hydrograph and flow depth variation during the reconstructed event in December 2009. Note the good agreement between the observed (solid line) and simulated (coloured area) flood extent in panels (b), (d) and (f).

soil surface, we could obtain high-quality simulations. Recall that there are a relatively small number of simulations with CSI > 0.7 (Wood et al., 2016).

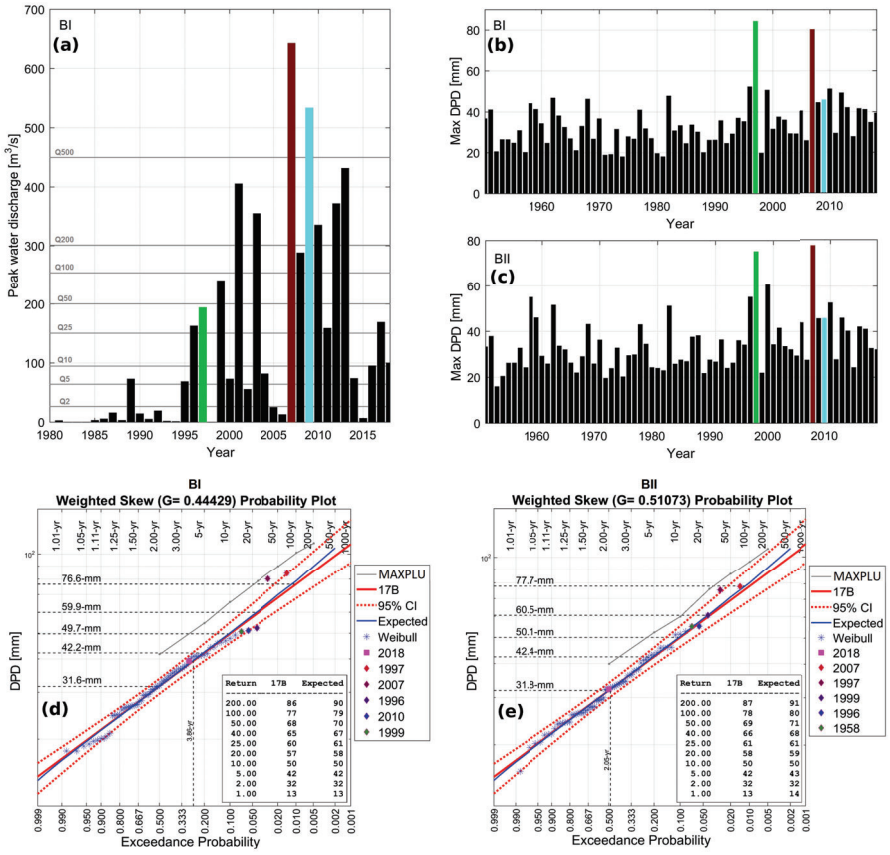

Fig. 4 (a) Annual peak discharge recorded in BI during the period 1981-2018. The events commented in the text are coloured in green (1997), brown (2007) and light blue (2009). The horizontal grey lines represent the values for return periods between 2 and 500 yr (CEDEX, 2014). (b)-(c) Maximum daily precipitation depth (DPD) in the period 1951-2019 for (a) BI and (b) BII. Data source: AEMETv2 (Peral-García et al., 2017). (d)-(e) Frequency analysis of DPD in BI-BII using PeakFQ (Veilleux et al., 2014).

Furthermore, the accuracy in the current agricultural areas is even better than in our previous set-up which included confined valleys and urban floodplains in meandering channels with $0.80 \leq \text{CSI} \leq 0.84$ (Bohorquez, 2016; Bohorquez and del Moral-Erencia, 2017).

Subsequently, we evaluated the rainfall intensity parameter (2) using the peak water discharge PMF = 533 $m^3 \cdot s^{-1}$ recorded at the gauge station and obtained PMP = 2.9 $mm \cdot h^{-1}$. The theoretical value of the minimum duration of the event given by the time of concentration (3) was T = 7.1 h. There is a close agreement with the inferred value of 7.5 h from the recorded hydrograph (inset of Fig. 3b) because the relative error is only 5%. The minimum precipitation depth accumulated during this period ($T \times PMP = 20.6$ mm) is consistently lower than the daily precipitation (i.e. DPD = 44.4 mm) given

by AEMETv2 (Peral-García et al., 2017), see Table 2, as the real rainstorm lasted more than 10.5 h. From flood risk analysis, the longer duration of the hydrological event does not increase the 533 $m^3 \cdot s^{-1}$ peak discharge, which was sustained for 3 h (inset of Fig. 3b), nor the extent of the inundation areas.

The importance of short-rain versus long-rain floods is evident regarding the magnitude of the ensuing discharge (Fig. 4a). Indeed, long-rain floods in 1997 and 2007, with daily precipitation depths (> 80 mm) doubling the value of the 2009 short-rain flood (44.4 mm), led to much lower (240 $m^3 \cdot s^{-1}$) or similar discharges (643 $m^3 \cdot s^{-1}$), respectively. Even the recurrence intervals of the flood magnitude and the daily precipitation are poorly related. DPD in 1997 and 2007 exhibited exceptional 50-100 yr return periods (Fig. 4d), but the discharge recurrence interval was 50-500 yr (Fig. 4a). In the reconstructed event of 2009, the return periods of DPD and PMF were 3.8 yr and 500 yr, respectively. The reconstruction of short-rain floods in ungauged basins is therefore important because the existing rainfall database does not capture their developments.

3.2 Inverse Problem in a Complex Floodplain (BII)

We now consider the inverse problem that consists of reconstructing the peak streamflow and rainfall intensity from the observed inundation map in an intricate floodplain where multiple streams merge. The inundated region was first delimited mainly by remotely sensed slackwater sediments. As in the previous study case, slackwater sediments were the dominant PSIs in the aerial orthophotos (yellow region in Fig. 3e). They occupied the 78% of the floodplain, while young grass (12%), secondary channels (8%) and scoured trees (2%) were less probable.

The hydrological event that provoked the flood was the same as studied in Section 3.1 given the proximity of basins BI and BII (Fig. 1b). In the floodplain of BII, there are three torrents (whose inlets are denoted by I1, I3 and I4 in Fig. 3e) discharging into the main fluvial course (inlet I2). The flow resulting from the inundation of the floodplain is unconfined and developed a length (200-650 m) much longer than the bankfull width of the main channel (27 m). To match the observed wetted perimeter in the numerical simulation, we systematically varied the water discharge at the four inlets and prescribed the observed water stage at the outlet (denoted by O1 in Fig. 3e).

The CSI reached the maximum value of 0.91 with the inflows $\mathrm{PMF}_{I1} = 195$, $\mathrm{PMF}_{I2} = 180$, $\mathrm{PMF}_{I3} = 45$ and $\mathrm{PMF}_{I4} = 40$ $m^3 \cdot s^{-1}$. At the outlet, the total water discharge was PMF_{01}=460 $m^3 \cdot s^{-1}$. In the main river, the flow developed the maximum depth of the order of 5 m (Fig. 3f). Conversely, it was generally very shallow (i.e. ≤ 0.5 m) in the floodplains, though the erosion of secondary channels induced deeper flows of about 2 m. High-speed flows with characteristic velocities of $2 - 3$ $m \cdot s^{-1}$ eroded fine sediments in the floodplain and sculpted several secondary channels parallel to the main stream and tributaries (Fig. 3e). The velocity was also high in the main channels (i.e.

$\geq$ 2 m·s^{-1}), which transferred sediments downstream. Flow velocities lower than 0.5 m·s^{-1} are consistent with the presence of slackwater sediments near the shorelines.

Subsequently, PMP (2) in each sub-basin was PMP_{I1} = 8.1, PMP_{I2} = 3.4, PMP_{I3} = 10.6 and PMP_{I4} = 10.5 mm·h^{-1} for the drainage areas given in Table 2. The variation of the inferred rainfall intensities across BII indicates the existence of short-range torrential processes during the event. The average intensity in BII was PMP_{O1} = 5.4 mm·h^{-1} over 307 km^2. The minimum duration of the event (3) was T = 5.6 h, which yields a minimum precipitation depth of T × PMP = 30.2 mm. Again, our result is consistently lower than the 45.7 mm daily precipitation depth by AEMETv2 (Peral-García et al., 2017), which is nearly the same as in BI (Table 2). Note that the trends of the DMP records from AEMETv2 are the same in BI (Fig. 4b) and BII (Fig. 4c).

As reported in BI, the 5 yr DPD recurrence period (Fig. 4e) significantly differs respect to the probability of the reconstructed peak discharge. According to the national CAUMAX database (CEDEX, 2014), the recurrence interval of the 2009 event is much higher than 500 yr because of PMF = 307 $\gg$ PMF_{500} = 199 m^3·s^{-1} (Table 2). The studied rainfall event was extreme in BII. Indeed, the rainfall intensity in BII (5.4 mm·h^{-1}) was nearly the double of BI (2.9 mm·h^{-1}). The peak discharge in both basins were around 500 m^3·s^{-1} but the drainage area of BII is half of BI. The spatial variation of the rainstorm, however, cannot be observed in the existing DPD database by AEMETv2 probably due to its coarse spatial resolution (5 km) and the lack of a denser rain gauge network in BI-BII (there are only 6 pluviometers). Our analysis points out the necessity of local detailed flood studies with a high-spatial-resolution. The current methodology can be straightforwardly applied in other catchments of the Guadalquivir Basin to construct a novel database of PMP and T suitable for short-rain flood risk analysis.

3.3 Inverse Problem in a Steep Torrential Ungauged Basin (BIII)

In this section, we consider the application and verification of the inverse method in a steep-slope, torrential, ungauged basin (23.3 km^2) and four tiny sub-basins (0.26-1.54 km^2), as shown in Fig. 5a. The small drainage area requires a notable increase in the spatial resolution regarding BI-BII. In contrast to the previous basins, the inundated region was delimited by erosive rather than depositional processes because the steep slope provoked high shear-rates in the floodplains. Furthermore, the most extreme rainfall event in BIII since 1946 occurred in September 2009 according to surrounding rain-gauge measurements (Fig. 5), which also differs from BI-BII.

The resolution of the inverse problem (black arrow in Fig. 2) was undertaken by delimiting the perimeter of scoured trees (89% of the total HWM-PSIs) and the growth of young grass (11%) at the outlet river stretch (Fig. 5b). The retrodicted values given in Table 2 are PMF = 170 m^3·s^{-1}, PMP = 26.3 mm·h^{-1} (2), T = 1.9 h (3) and T × PMP = 49.9 mm with a

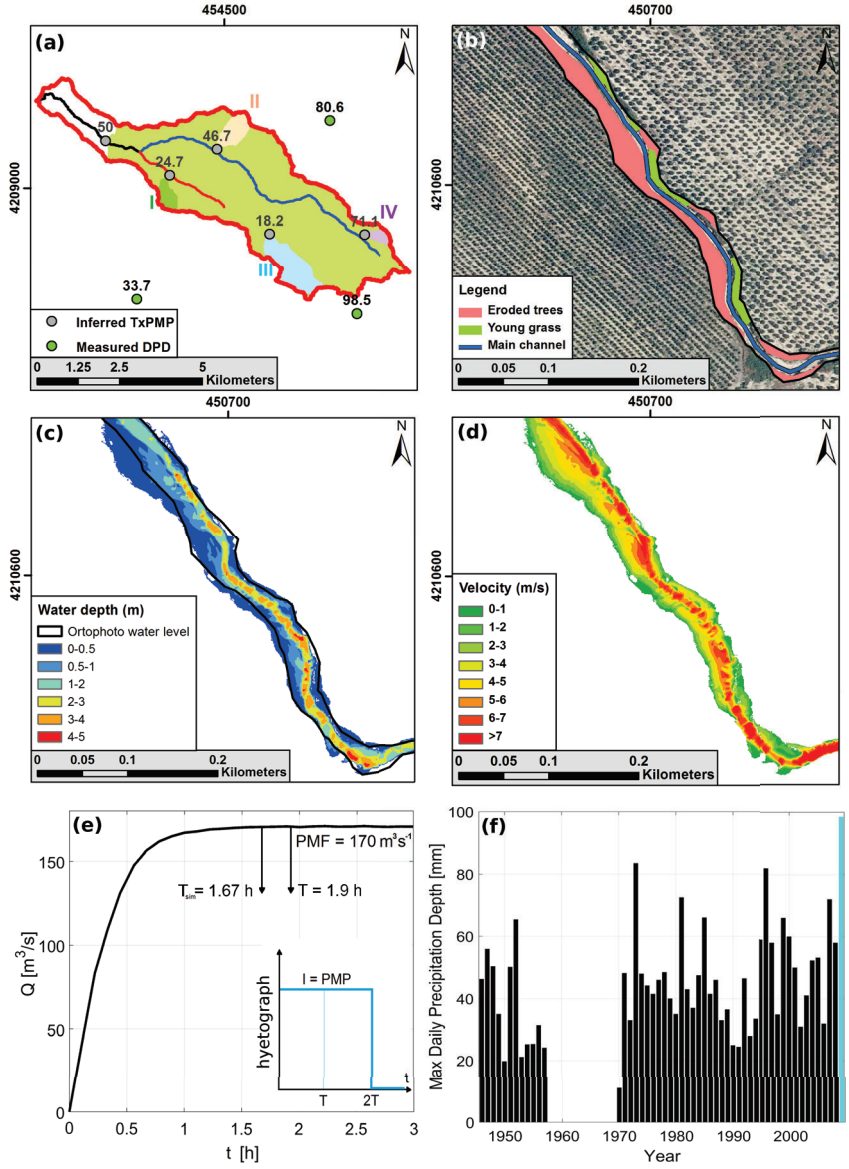

Fig. 5 (a) Minimum precipitation depth (mm) required for the observed inundation (T×PMP, grey circles) and measured daily values (DPD, green circles) in BIII. (b) Remote-sensed flooded area from local orthophotos (PNOA, 07/2011), (c) simulated water depth and (d) velocity magnitude for the inferred discharges PMF=170 $m^3 \cdot s^{-1}$ at the outlet of BIII. (e) Hydrograph computed at the outlet of BIII by simulating numerically the rainfall-runoff process in the whole catchment with Iber+. (f) Annual maximum DPD measured in a gauge near the headwaters of BIII for the period 1946-2010, showing the studied event in light blue.

success index of CSI = 0.77 (1). The simulated water depth (Fig. 5c) and the magnitude of the velocity vector (Fig. 5d) explains the absence of depositional evidence in the observed PSIs (Fig. 5b). Indeed, the velocity in the eroded floodplains was remarkably high (2-4 $m \cdot s^{-1}$), explaining the scouring of trees. The deepest flows (3-5 m) and highest velocities (6-7 $m \cdot s^{-1}$) developed in the main channel.

Inspired by Bellos and Tsakiris (2016), we verified the inferred results from the paleohydrological/rational-method through the direct numerical simulation of the *S*-hydrograph using the distributed rainfall-runoff model Iber+ by García-Feal et al. (2018). We referred this step in the sketch of Fig. 2 as direct calculation (red arrow). We set a continuous rainfall excess at a constant rate PMP for a period of 2T as input hyetogram (inset of Fig. 5e). The most accurate representation of the real topography of the whole basin was achieved using an unstructured mesh with 603375 elements and a cell size of 1.5 m as thin as the average distance between the LiDAR points. Figure 5e shows the output hydrograph at the river stretch where the paleohydrological reconstruction was undertaken (Figs. 5b-d). Interestingly, the discharge achieved the value of PMF (i.e. 170 $m^3 \cdot s^{-1}$) at the instant of time T_{sim} = 1.67 h. The relative difference concerning the theoretical time of concentration given by the rational method T = 1.9 h (3) is, therefore, 12%. Such a slight difference might be due to the simple estimation of the characteristic length L in (3)-(4) as the length of the maximum axis because the basin was not square (i.e. $L \neq A_{drain}^{1/2}$). We conclude that the incorporation of recent technological advances as high-resolution LiDAR elevations and GPU-accelerated numerical codes for hydrological calculations allowed us to establish the accuracy and applicability of the rational method in the basins.

Subsequently, we applied the inverse method recursively in the sub-basins I-IV depicted in Fig. 5a. Results are summarised in Table 2. The maximum and minimum PMP were 37.4 and 9.6 $mm \cdot h^{-1}$, respectively. Note the considerable irregularity of the precipitation intensity over BIII. The maximum absolute deviation was of the same order as the average value. Though we could not undertake a quantitative comparison against experimental measurements (due to the absence of rain gauge data with a sampling rate lower than 24 h), the inferred precipitation depths (T×PMP) show qualitatively the same geographical distribution and variation than the measured DPD in rain gauges nearby (Fig. 5a). The complex topography may lead to orographic precipitation processes during torrential phenomena. The incorporation of the spatial variability of the precipitation into the distributed hydrological model Iber+, coupled with uncertainty analysis (Bellos et al., 2020), could improve the flood risk analysis in the catchment scale.

Additionally, the analysis of the maximum DPD since the middle of the twentieth century indicates an increase from the 1990s, specifically in events with DPD > 50 mm (Fig. 5f). The highest peak corresponds to the studied event, indicated in light blue colour. The events recorded in BIII are different than in BI-BII due to the geographical distance between basins. Despite this fact, the observed growing tendency in terms of DPD is very similar.

Finally, we estimated the amount of sediment transferred from the watershed as the total volume of eroded sediments by overland flows. We excluded deep gullies and streams that behave as zones of sediment transfer. The soil erosion rate in the remaining area of the basin was evaluated through a dimensionless erosion law for the dominant sand-mud cohesive mixture (Walder, 2015), which yields the mean value $\bar{E} = 0.42$ m·h^{-1}. We also run the hydrological model in BI and BII obtaining, respectively, $\bar{E} = 0.057$ and 0.046 m·h^{-1}. These erosion rates are one order of magnitude smaller than in BIII. Multiplying $\bar{E}$ by the eroded area and the duration of the event yields the sediment budgets of 16.8 (BI), 15.7 (BII) and 0.47 Mm^3 (BIII).

4 Conclusions

The characterisation of short-rain floods at local scale, $A_{\text{drain}} \sim 10^3$ km^2, is necessary for basins in southern Spain due to their increasing frequency and magnitude (PMF ~ 500 m^3·s^{-1}). Their short time to peak flow, T$<$ 24h, and substantial spatial variation enforce the development of a new methodology to reconstruct the flood dynamics in ungauged basins. Indeed, available (daily) rainfall databases at the national scale do not capture the precipitation intensity of sub-daily events, and the analysis of peak discharges show that recent short-rain floods are uncorrelated at the basin scale. Also, a significant mismatch exists between the recurrence intervals of flood magnitude and daily precipitation depth.

The paleohydrology reconstruction incorporates remote-sensed paleostage indicators to infer the river discharge PMF, and the rational method for the spatio-temporal averaged rainfall intensity PMP and minimum event duration T. The verification with gauged data, and a distributed hydrological software, draw low relative errors ($10 - 23\%$). The recursive application of the method in sub-basins may achieve a spatial resolution $<$1 km. The future purpose is to create an original PMF, PMP and T database for short-rain floods in other catchments of the Guadalquivir Basin, which is required to properly apply the Spanish Directive FOM/298/2016 (https://www.boe.es/) for the construction of safety drainage systems in civil works. At the European scale, the implementation of the methodology is appropriate in basins with similar physical characteristics around the Mediterranean region.

Under the current climate change scenario in the Guadalquivir Basin, the increase in discharge of sub-daily floods in tributaries contrast with a decrease in the magnitude of long-rain floods (T$\approx$7d) at the whole basin (Bohorquez, 2016). The increase in extreme events across tributary basins provoked a high-incidence of erosive processes and larger sediment budgets. Such phenomena are linked to sedimentation processes, reduction in channel capacity and higher flood risk in the main Guadalquivir River despite the decrease in maximum discharge (Bohorquez and del Moral-Erencia, 2017). A probable treatment plan to reduce the impact of erosion due to climate change could implement natural flood management measures over the basin. Recommended mechanisms are sediment traps and in-gully barriers,

alternating organic groves between conventional soils with till farms, bunds and detention areas, and restoration of ephemeral wetlands, among others. Such interventions contribute to interrupting surface flows of water and sediment, increasing soil infiltration, storing water and slowing water by increasing resistance to its flow.

Acknowledgements This work was supported by the Spanish Ministry of Science, Innovation and Universities (MICINN/FEDER, UE) under Grant SEDRETO CGL2015-70736-R. J.D.d.M.E. was supported by the PhD scholarship BES-2016-079117 (MINECO/FSE, UE) from the Spanish National Programme for the Promotion of Talent and its Employability (call 2016).

Conflict of interest

The authors declare that they have no conflict of interest.

References

Alfieri L, Thielen J (2015) A European precipitation index for extreme rain-storm and flash flood early warning. Meteorol Appl 22(1):3–13, https://doi.org/10.1002/met.1328

Alfieri L, Berenguer M, Knechtl V, Liechti K, Sempere-Torres D, Zappa M (2016) Flash flood forecasting based on rainfall thresholds. In: Duan Q, Pappenberger F, Thielen J, Wood A, Cloke HL, Schaake JC (eds) Handbook of Hydrometeorological Ensemble Forecasting, Springer Berlin Heidelberg, Berlin, Heidelberg, pp 1–38, https://doi.org/10.1007/978-3-642-40457-3_49-1

Baker V (2008) Paleoflood hydrology: Origin, progress, prospects. Geomorphology 101(1-2):1–13, https://doi.org/10.1016/j.geomorph.2008.05.016

Bates P, De Roo A (2000) A simple raster-based model for flood inundation simulation. J Hydrol 236(1-2):54–77, https://doi.org/10.1016/S0022-1694(00)00278-X

Bellos V, Papageorgaki I, Kourtis I, Vangelis H, Kalogiros I, and Tsakiris G (2020) Reconstruction of a flash flood event using a 2D hydrodynamic model under spatial and temporal variability of storm. Nat Hazards, https://doi.org/10.1007/s11069-020-03891-3

Bellos V, Tsakiris G (2016) A hybrid method for flood simulation in small catchments combining hydrodynamic and hydrological techniques. J Hydrol 540:331–339, https://doi.org/10.1016/j.jhydrol.2016.06.040

Bodoque J, Díez-Herrero A, Martín-Duque J, Rubiales J, Godfrey A, Pedraza J, Carrasco R, Sanz M (2005) Sheet erosion rates determined by using dendrogeomorphological analysis of exposed tree roots: Two examples from Central Spain. Catena 64(1):81–102, https://doi.org/10.1016/j.catena.2005.08.002

Bohorquez P (2016) Paleohydraulic reconstruction of modern large floods at subcritical speed in a confined valley: Proof of concept. Water 8(12), https://doi.org/10.3390/w8120567

Bohorquez P, Darby S (2008) The use of one- and two-dimensional hydraulic modelling to reconstruct a glacial outburst flood in a steep Alpine valley. J Hydrol 361(3-4):240–261, https://doi.org/10.1016/j.jhydrol.2008.07.043

Bohorquez P, del Moral-Erencia J (2017) 100 years of competition between reduction in channel capacity and streamflow during floods in the Guadalquivir River (Southern Spain). Remote Sens 9(7), https://doi.org/10.3390/rs9070727

Brutsaert W (2005) Hydrology: An Introduction. Cambridge University Press, https://doi.org/10.1017/CBO9780511808470

Carling PA, Herget J, Lanz JK, Richardson K, Pacifici A (2009) Channel-scale erosional bedforms in bedrock and in loose granular material: Character, processes and implications. In: Burr, D M, Carling, P A, Baker, V R (eds) Megaflooding on Earth and Mars, Cambridge University Press, Cambridge, pp 13–32, https://doi.org/10.1017/CBO9780511635632.002

CEDEX (2014) Mapa de Caudales Máximos. Memoria Técnica. Dirección General del Agua. Ministerio de Agricultura y Pesca, Alimentación y Medio Ambiente, NIPO: 770-11-273-7

Díez-Herrero A, Laín-Huerta L, Llorente-Isidro M (2008) Mapas de peligrosidad por avenidas e inundaciones. Guía metodológica para su elaboración. No. 1 in Riesgos geológicos / Geotecnia, Publicaciones del Instituto Geológico y Minero de España, Madrid, ISBN: 978-84-7840-770-5

Dottori F, Szewczyk W, Ciscar JC, Zhao F, Alfieri L, Hirabayashi Y, Bianchi A, Mongelli I, Frieler K, Betts R, Feyen L (2018) Increased human and economic losses from river flooding with anthropogenic warming. Nat Clim Chang 8(9):781–786, https://doi.org/10.1038/s41558-018-0257-z

EEA (2017) Climate change, impacts and vulnerability in Europe 2016: An indicator-based report. Publications Office of the European Union, Luxembourg, 1/2017, https://doi.org/10.2800/534806

García-Feal O, González-Cao J, Gómez-Gesteira M, Cea L, Domínguez J, Formella A (2018) An accelerated tool for flood modelling based on Iber. Water 10(10), https://doi.org/10.3390/w10101459

IPCC (2013) In: Stocker, TF, Qin, D, Plattner, GK, Tignor, MMB, Allen, SK, Boschung, J, Nauels, A, Xia, Y, Bex, V, Midgley, PM (eds) Climate Change 2013: The Physical Science Basis. Contribution of Working Group I to the Fifth Assessment Report of the Intergovernmental Panel on Climate Change, Cambridge University Press, Cambridge, UK, ISBN: 978-92-9169-138-8

Jacobson RB, O'Connor JE, Oguchi T (2016) Surficial geological tools in fluvial geomorphology. In: Tools in Fluvial Geomorphology, John Wiley & Sons, Ltd, pp 11–39, https://doi.org/10.1002/9781118648551.ch2

Mays LW (2010) Water Resources Engineering, 2nd edn. John Wiley & Sons, Ltd, ISBN: 978-0-470-46064-1

Merz R, Blöschl G (2003) A process typology of regional floods. Water Resour Res 39(12):SWC51–SWC520, https://doi.org/10.1029/2002WR001952

Naylor L, Spencer T, Lane S, Darby S, Magilligan F, Macklin M, Möller I (2017) Stormy geomorphology: geomorphic contributions in an age of climate extremes. Earth Surf Process Landf 42(1):166–190, https://doi.org/10.1002/esp.4062

Peral-García C, Fernández-Victorio BN, P RC (2017) Serie de precipitación diaria en rejilla con fines climáticos. Agencia Estatal de Meteorología, Ministerio de Agricultura y Pesca, Alimentación y Medio Ambiente, NIPO: 014-17-009-5

Veilleux AG, Cohn TA, Flynn KM, Mason Jr RR, Hummel PR (2014) Estimating magnitude and frequency of floods using the PeakFQ 7.0 program. Report 2013-3108, Reston, VA, https://doi.org/10.3133/fs20133108

Walder J S (2015) Dimensionless erosion laws for cohesive sediment. J Hydraul Eng 142(2): 04015047, https://doi.org/10.1061/(ASCE)HY.1943-7900.0001068

Wood M, Hostache R, Neal J, Wagener T, Giustarini L, Chini M, Corato G, Matgen P, Bates P (2016) Calibration of channel depth and friction parameters in the LISFLOOD-FP hydraulic model using medium-resolution SAR data and identifiability techniques. Hydrol Earth Syst Sci 20(12):4983–4997, https://doi.org/10.5194/hess-20-4983-2016